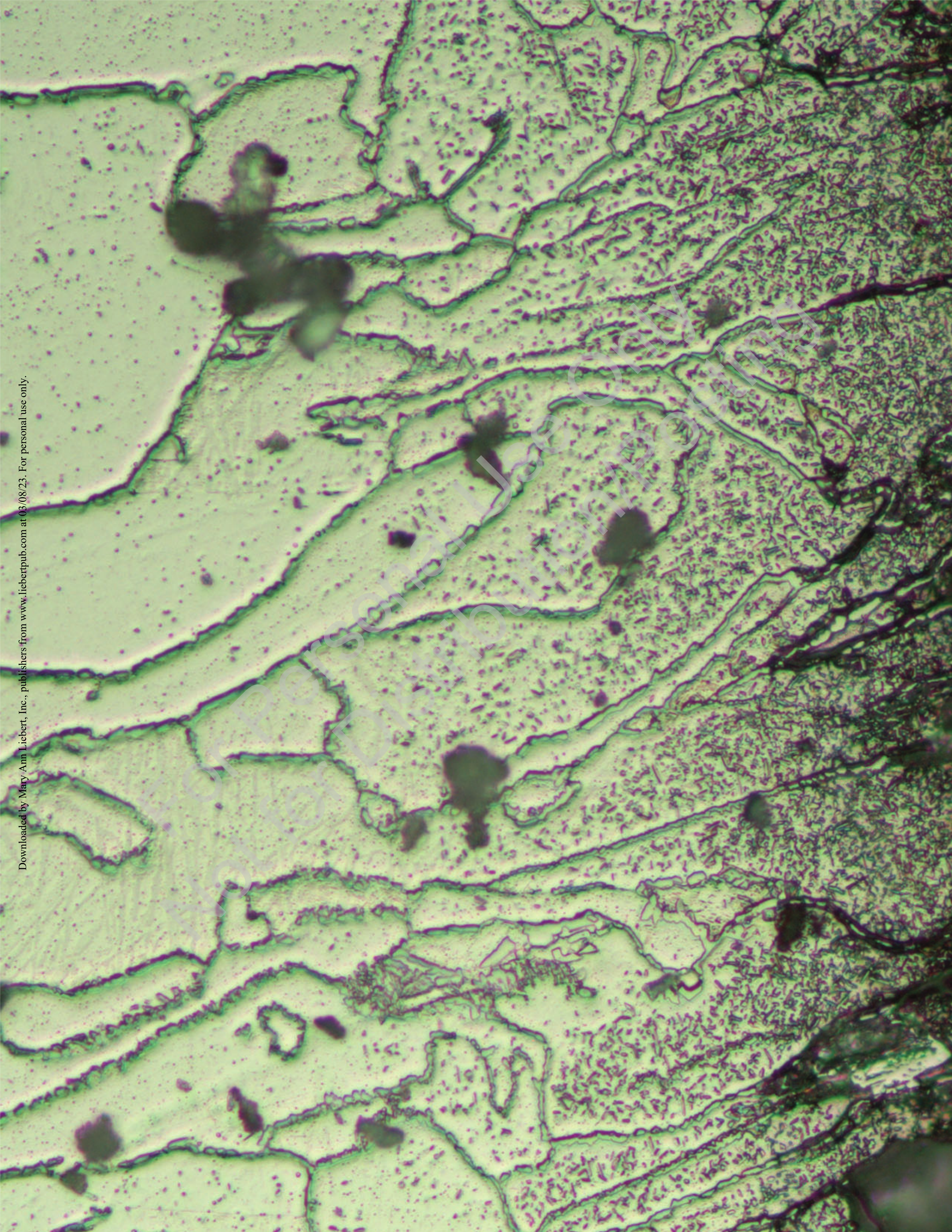

3D PRINTING AND ADDITIVE MANUFACTURING
Volume 00, Number 00, 2022

DOI: 10.1089/3dp.2022.0190

Effect of Microstructure and Dislocation Density on Material Removal and Surface Finish of Laser Powder Bed Fusion 316L Stainless Steel Subject to a Self-Terminating Etching Process

Stephanie Prochaska,[1] Michael Walker,[3] and Owen Hildreth[2]

Abstract

Postprocessing of additively manufactured (AM) metal parts to remove support structures or improve the surface condition can be a manually intensive process. One novel solution is a two-step, self-terminating etching process (STEP), which achieves both support removal and surface smoothing. While the STEP has been demonstrated for laser powder bed fusion (L-PBF) 316L stainless steel, this work evaluates the impact of pre-STEP heat treatments and resulting changes in dislocation density and microstructure on the resulting surface roughness and amount of material removed. Two pre-STEP heat treatments were evaluated: stress relief at 470°C for 5 h and recrystallization–solution annealing at 1060°C for 1 h. Additionally, one set of specimens was processed without the pre-STEP heat treatment (as-printed condition). Dislocation density and phase composition were quantified using X-ray diffraction along with standard, metallurgical stain-etching techniques. This work, for the first time, highlights the mechanisms of sensitization of AM L-PBF 316L stainless steel and provides fundamental insights into selective etching of these materials. Results showed that the sensitization depth decreased with increasing dislocation density. For samples etched at a STEP bias of $540\,\mathrm{mV_{SHE}}$, material removal terminated at grain boundaries; therefore, the fine-grained stress-relieved specimen had the lowest post-STEP surface roughness. For surface roughness optimization, parts should be stress relived pre-STEP. However, to achieve more material removal, pre-STEP solution annealing should be performed.

Keywords: microstructure, dislocations, electrochemical etching, surface finishing, self-terminating etching process, sensitization

Introduction

Postprocessing is a large cost driver of additively manufactured (AM) metal components.[1] Bulk surface finishing and elimination of support structures remain a challenge, particularly when part geometries are complex and difficult to access with manual removal processes. One novel self-terminating etching process (STEP) aims to solve these issues by selectively sensitizing and electrochemically etching away the top 50–200 lm of a metal part, including support structures if they are designed to be thinner than the sensitized region.[2,3]

In the STEP for stainless steel alloys, parts are coated with sodium hexacyanoferrate, which decomposes to form carbon during an annealing process. The carbon diffuses through the surface and forms chromium carbide precipitates, effectively sensitizing the part's surface by reducing the amount of free chromium available to form a protective passivation layer.

Depending on processing conditions, this "sensitized" region is often between 50 and 200 lm thick. The component is then etched under a specific bias such that the sensitized region corrodes away, while the cathodic bulk is preserved. The STEP has

---

[1] Materials Science Program, Colorado School of Mines, Golden, Colorado, USA.
[2] Department of Mechanical Engineering, Colorado School of Mines, Golden, Colorado, USA.
[3] Department of Metallurgical and Materials Engineering, Shared Instrumentation Facilities, Colorado School of Mines, Golden, Colorado, USA.

Opposite page: 31.5x cross-sectional micrograph of the near-surface microstructure of the Solution Annealed, Etched (SA-E) specimen. The corrosive attack accentuated the SA-E specimen's coarser structure. Specimens were stain etched with glyceregia for 80 seconds. Image Credit: Stephanie Prochaska, PhD; Hildreth Lab.

been validated for AM laser powder bed fusion (L-PBF) 316L stainless steel components in the as-printed (AP) condition.[2,4,5]

However, it was not clear if the STEP should be applied immediately after printing, after stress relief, or after recrystallization. The microstructure changes associated with each of these steps can be expected to impact the resulting sensitized microstructure and ultimate process outcomes of surface roughness and amount of material removed.

AP AM microstructures are complex with nanoscale columnar and cellular grains crossing melt pool boundaries, among other unique features.[6–8] Rapid solidification induces high densities of cellular dislocation networks.[9] These networks disrupt the chemical homogeneity of the microstructure and should impact the sensitization and corrosion response of the material.

Prior STEP studies on AP L-PBF 316L have shown both intragranular and intergranular diffusion of carbon, with etching bias controlling whether the subsequent dissolution of the sensitized region targets the grain boundaries or is uniform across the surface.[5] Otherwise, the effect of component microstructure (grain size, shape, and uniformity) on the STEP carbon diffusion length/sensitization distance, amount of material removed, and resulting surface roughness has been largely unstudied.

In addition, the residual stresses and high dislocation densities, inherent to the printing process' thermal gradients and rapid cooling rates, are commonly resolved through a postbuild stress relief heat treatment.[10] Dislocations are known to impact the kinetics of diffusing species by either acting as barriers to impede their movement or facilitating it through acting as express channels,[11–13] but their role in STEP is currently undetermined.

While stress relief improves mechanical properties of parts, the relatively low temperature utilized does not induce a microstructural change in L-PBF 316L parts. Alternatively, parts may be subjected to solution annealing, which recrystallizes the microstructure, resolves dislocations, and further improves properties such as fatigue performance and tensile strength.[14]

The aim of this study is to determine the effects of microstructure and dislocation density on the STEP, focusing on impacts on carbon diffusion length, material removal (etching), and resulting surface roughness. To evaluate the effect of decreased dislocation density on sensitization depth, 316L stainless steel disks were subjected to a stress relief heat treatment before the STEP. To evaluate the effect of microstructural changes, disks were solution annealed (SA) at a temperature that recrystallized the microstructure before the STEP. Finally, AP disks that were subjected to the STEP were also evaluated.

Experimental analysis

Specimen preparation

An EOS M 290 Direct Metal Laser Sintering system printed specimen disks, 15 mm in diameter and 7 mm thick, from 316L stainless steel powder. After being removed from the build platform, the final disk thickness was 4 mm. Disks were oriented with their circular face parallel to the XY direction on the build platform. The printing parameters were laser power of 214.2 W, scan speed of 928.1 mm/s, hatch spacing of 100 lm, and layer thickness of 40 lm.

Auger electron spectroscopy characterized the chemical composition of the printed disks (Table 1), which meets the specification standard for 316L stainless steel.[15]

Table 1. Chemical Composition of Printed 316L Disks in wt.% (Balance Fe)

Material	C	Cr	Mn	Mo	Ni	P	S	Si
L-PBF 316L	0.020	17.65	0.67	2.40	13.15	0.011	0.010	0.62

L-PBF, laser powder bed fusion.

Heat treatments. Disk specimens were subjected to one of two thermal treatments, the stress relief treatment or recrystallization–solution annealing. Stress-relieved (SR) specimens were heat-treated in an argon gas environment in a Lindberg Model C10 silicon carbide box furnace at 470°C for 5 h, followed by overnight furnace cooling to room temperature. SA specimens were annealed at 1060°C for 1 h in an argon gas environment in a Thermo Scientific Lindberg Blue M tube furnace and were subsequently ice water quenched.

The furnace ramp rate was 10°C/min and heat treatments were pursuant to ASTM F3184.[16] A third set of specimens were not subjected to any postbuild heat treatments and were evaluated in the AP condition. Six specimens of each treatment type were prepared for analysis.

Self-terminating etching process. To evaluate the effects of microstructure and dislocation density on the STEP, SR and SA disks were subjected to STEP after the heat treatment. For comparison, AP disks were also subjected to STEP. For stainless steel, STEP consists of two successive parts: sensitization and chemical etching.[2,4]

To sensitize the disk specimens, they are first submerged in a saturated solution of sodium hexacyanoferrate (II) decahydrate $[Na_4Fe(CN)_6\$10H_2O]$ and deionized water for 20 min at room temperature. Internal channels and support structures are sensitized as long as the solution is in contact with the base metal in those regions. After removal from the solution, parts are coated with a 4.2:1 paste of $Na_4Fe(CN)_6\$10H_2O$ and deionized water (18 MO, Thermo Scientific Smart2Pure 3 UV/UF).

A layer of graphite powder is spread onto a high-temperature 309 stainless steel tool wrap, the parts coated in the slurry are laid on top, and another layer of graphite powder is applied to completely cover the parts and paste. The tool wrap is tightly folded to form a package and 0.1-mm-diameter holes are punched in the corners to allow the release of cyanide and water vapor formed during paste decomposition.

A silicon carbide box furnace performs the three-step sensitization process. First, with the package inside, the furnace is vacuum purged and backfilled with argon gas for three cycles at room temperature. Second, a dehydration process ramps the furnace at a rate of 5°C/min to 90°C, followed by a 40-min dwell time, then ramps it to 185°C with a dwell time of 60 min, and finally ramps it to 250°C with a dwell time of 60 min. In the last step, the furnace is ramped at 5°C/min to 915°C. Third, after dwelling at 915°C for 7 h, the package is ice water quenched to room temperature. Samples are ultrasonicated in deionized water for 5 min to remove the remnant paste and graphite.

The electrochemical etching procedure involves performing chronoamperometry on the samples with an Applied Research Parstat MC potentiostat at an applied potential of 540 mV_{SHE} for 50 h in a solution of 0.48 molar concentration of nitric acid (HNO_3) and 0.1 molar concentration of potassium chloride (KCl).[5] A stainless steel wire is wrapped around the disk specimen edges, and together, the wire and specimen form the working electrode. A 4 M KCl salt bridge ionically connects a sliver/silver chloride reference electrode to the electrolyte, and a 6.35-mm-diameter graphite rod is the counter electrode. Once the chemical etching is complete, specimens are ultrasonicated in isopropyl alcohol for 30 min.

Specimen evaluation

In total, this work evaluated nine different specimen types, as listed in Table 2 with the type of heat treatment applied and subsequent step in the STEP at which specimens were evaluated.

The specimen IDs have two parts—the first two letters indicate whether the samples received any heat treatment before the STEP was applied. AP indicates that the samples were subjected to STEP in the ''as-printed'' state. SR indicates that the sample was stress relieved before the STEP, and SA indicates that the sample was SA before the STEP.

The second set of letters denotes where the sample is along the STEP sequence, with AB denoting an ''as-built'' condition, S indicating that the samples were sensitized, and E indicating that the samples were sensitized and subsequently electrochemically etched.

X-ray diffraction measurements and peak profile analysis. X-ray diffraction (XRD) patterns for the AB disk specimens were collected on a Bruker AXS D2 Phaser diffractometer with a Co Kα source. XRD patterns were also collected from a cold rolled 316L specimen. To record a high-resolution scan, the dwell time at each 0.02° step was 4 s through an angular range of 27° to 130° two theta.[17] A lanthanum hexaboride powder line and peak broadening standard reference material (660a) obtained from the National Institute of Standards and Technology calibrated the XRD's profile function, and the XRD analysis software, HighScore (Malvern Panalytical, Malvern, UK), performed a Rietveld refinement to fit the standardized data to experimentally collected data.[18]

Crystallite size and strain were calculated for each specimen during the fitting procedure in addition to the interplanar spacing (d_{hkl}) and integral breadth (°2θ) for each peak. A Williamson–Hall analysis was performed where each specimen's peaks are plotted as $\beta\cos\theta$ versus $\sin\theta$ to obtain a corresponding linear trend line and equation.[19] The trend line's slope corresponds to the microstrain, ε. To calculate dislocation density, ρ_D, Equation (1) is used[20,21]:

Table 2. Specimen IDs Based on Heat Treatment and the Part of the Self-Terminating Etching Process Sequence That Has Been Completed

	STEP		
	As-built	Sensitized	Electrochemically etched
As-printed	AP-AB	AP-S	AP-E
Stress relief	SR-AB	SR-S	SR-E
Solution annealing	SA-AB	SA-S	SA-E

AB indicates the as-built condition, S indicates that specimens were sensitized, and E indicates that the samples were sensitized and chemically etched.

AP, as-printed; SA, solution annealed; SR, stress relieved; STEP, self-terminating etching process.

$$\rho_D = \frac{3\sqrt{2\pi}\,(\varepsilon^2)^{1/2}}{Db} \tag{1}$$

In Equation (1), D is the crystallite size and b is the magnitude of the Burgers vector. For face-centered cubic metals, the magnitude of the Burgers vector is calculated as $b = \frac{a\sqrt{2}}{2}$, where a is the unit cell edge length or lattice parameter. Lattice parameters were calculated for each peak through the formula, $a = d_{hkl}\sqrt{h^2 + k^2 + l^2}$, and subsequently averaged for each specimen type.

Microstructure and surface characterization. Specimen disks were cross-sectioned with a Leco MSX205 sectioning machine, cold-mounted in epoxy (EpoFix, Struers), and sequentially ground and polished to a one-micron finish with silicon carbide paper and diamond polishing suspensions (Leco). To reveal the general microstructure, specimens were stain etched with glyceregia (1:2:3 solution of HNO_3, glycerol, and hydrochloric acid) for 80 s.

For a second set of specimens, intragranular and intergranular carbides were etched in a solution of 10 g of oxalic acid in 90 mL of deionized water for 40 s under an applied potential of 6 V.[22] A Zeiss Axio Vert.A1 inverted optical microscope imaged the microstructures. A Bruker DektakXT contact profilometer quantified the surface roughness through six 5600-μm-long scans.

Three scans were perpendicular to the build direction and three were parallel to the build direction. The lateral resolution was 0.062 μm and stylus load was 3 mg. A short cutoff (λ_s) at 2.5 μm and a long cutoff (λ_c) at 0.8 mm filtered the data through a Gaussian regression.[23] The average total roughness profile, Ra, is reported for each specimen.

To evaluate differences in carbon diffusion after sensitization, carbon ion intensity curves were generated through time-of-flight secondary ion mass spectroscopy (TOF-SIMS) performed on the cross sections of sensitized samples, which were polished to a 1-μm finish with colloidal silica suspension and sputter-cleaned with argon at 10 keV.

The IonTOF TOF-SIMS V utilized a $Bi3^+$ primary ion at an energy of 30 keV, a 500-μm^2 field of view, and a 100-μs cycle time. Two successive 500-μm^2 scans were executed to achieve a total profile length of 1000 μm from the specimen edges into the bulk.

Results and Discussion

Peak profile analysis

The Rietveld and Williamson–Hall analyses assessed the effects of stress relief and solution annealing heat treatments on the microstrain, crystallite size, and dislocation density of L-PBF 316L stainless steel. Figure 1 shows the resulting plots and linear equations generated from the Williamson–Hall analysis on the AB and cold rolled specimens, and (Table 3) gives the extracted values for microstrain used to calculate dislocation density. Rietveld analysis results of the lattice parameter and crystallite size are also given in the table.

As expected, the cold rolled specimen has the highest strain and largest dislocation density of $2.64 \cdot 10^{15}\ m^{-2}$, validating the Williamson–Hall analysis method. Manufacturers typically apply cold working processes, such as cold rolling specifically, to generate and pin dislocations—resulting in a strengthened material with higher deformation resistance.

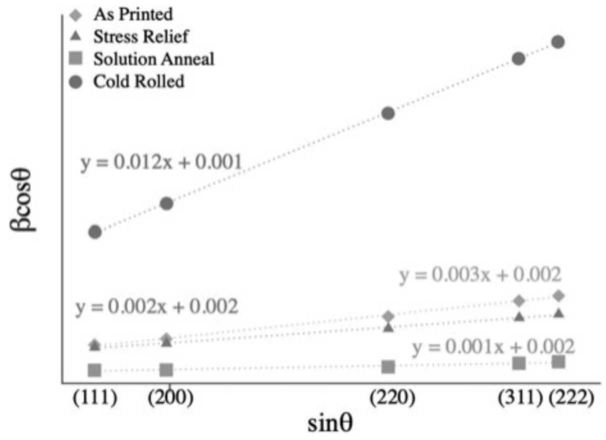

FIG. 1. Williamson–Hall plots of as-built AP, SR, and SA specimens and a cold rolled specimen. Trend line slope is the strain, the y-intercept is inversely proportional to the crystallite size, and dislocation density can be obtained from crystallite size. AP, as-printed; SA, solution annealed; SR, stress relieved.

L-PBF metals are a material that intrinsically has high dislocation densities due to thermal cycling during printing.

Exposure to elevated temperatures reduces dislocation density through dislocation climb and annihilation.[24,25] The stress relief heat treatment reduced the amount of strain and decreased the dislocation density from $0.68 \cdot 10^{15}\ \mathrm{m}^{-2}$ in the AP-AB specimen to $0.41 \cdot 10^{15}\ \mathrm{m}^{-2}$. As is common in heat treatments with long soak times, crystallites of the SR-AB specimen were correspondingly coarsened. The SA-AB specimen had the lowest strain, coarsest crystallites, and smallest dislocation density of $0.06 \cdot 10^{15}\ \mathrm{m}^{-2}$.

Microstructural evolution during the STEP also elicits changes to dislocation density. Dislocations are nucleation sites for carbide precipitation and also reduce the carbide growth time.[26]

Carbon diffusion depth

In austenitic stainless steel, carbide precipitation occurs intergranularly (along grain boundaries) and intragranularly (within the grains) when carbon concentrations are elevated and the steel is subjected to temperatures in the range of *510°C to 788°C.[15] Carbides precipitate intragranularly at defects, preferentially those related to strain, such as at dislocations.[27] Grain boundaries also act as preferential sites for carbide precipitation and are the preferential route for carbon diffusion.

Table 3. As-Built Specimen Crystallite Strain, Size, and Dislocation Density Values Obtained Through Williamson–Hall Analysis

	Rietveld		Williamson–Hall	
	Lattice parameter (Å)	Crystallite size (Å)	Microstrain (%)	Dislocation density ($\cdot 10^{15}\ \mathrm{m}^{-2}$)
Cold rolled	3.599	1345	1.20	2.64
AP-AB	3.600	1356	0.31	0.68
SR-AB	3.599	1501	0.21	0.41
SA-AB	3.600	2274	0.05	0.06

Therefore, grain size and shape impact the diffusion length. Minimizing the amount of intra- and intergranular carbides post-STEP is an important objective of this work. Figure 2 shows cross-sectional micrographs of the microstructure evolution through the STEP from the AB condition, to sensitization, and to the etched or post-STEP condition.

Each sensitized and etched micrograph shows two distinct inter- and intragranular regions of carbon diffusion. The intragranular region of all etched specimens is shorter in length than the intragranular region of sensitized specimens. This reduction in length represents the material removed during the chemical etching step in the STEP.

Quantification of the depths of intragranular and intergranular carbide regions is shown in Figure 3.

As-built specimens.

As discussed previously, the crystallite size of the AB specimens increases as follows: AP-AB < SR-AB < SA-AB. The minor coarsening between the AP-AB and SR-AB specimens is likely due to the prolonged time spent at an elevated temperature. The fine columnar and cellular structures are retained in the SR-AB specimen.

Solution annealing succeeded in coarsening the grains of the SA-AB specimen and, additionally, resulted in grains being more equiaxed than in the AP-AB and SR-AB specimens—this has been observed previously for L-PBF 316L stainless steel.[28] Solution annealing also completely dissolved fine columnar and cellular grains in the SA-AB specimen.

Dislocation densities decrease with longer heat treatment time and increasing temperature. The stress relief heat treatment was effective in reducing the dislocation density of the SR-AB specimen compared with the AP-AB specimen. The full solution annealing resulted in the SA-AB specimen having the lowest dislocation density of the AB specimens evaluated.

Sensitized specimens.

The sensitization temperature of 915°C refined the microstructures from the AB conditions, but is not high enough for complete recrystallization. The SA-S specimen retained much of its equiaxed nature from the AB condition, while the AP-S and SR-S specimen micrographs show large central grains flanked by attenuated needle-like grains. Grain size order (AP-S < SR-S < SA-S) is retained from the pre-STEP conditions.

The SA-S specimen had the longest intragranular carbon diffusion length of *374 lm and subsequently the longest total carbide diffusion depth of 574 lm. In contrast, the AP-S specimen's total diffusion depth was 501 lm, with the smallest intragranular depth of 240 lm. The SR-S specimen's total diffusion depth was 558 lm, with 340 lm of it being intragranular.

The AP-S specimen had the shortest intragranular carbide region of all specimens evaluated, followed by the SR-S specimen and then the SA-S specimen—thus indicating that the intragranular diffusion length decreases with increasing dislocation density. This trend continues for the cold rolled specimen, as seen at the bottom of Figure 2, which has the highest dislocation density.

The region of intragranular carbides in the sensitized cold rolled micrograph is similar in length to that of the AP-S specimen; however, the initial grain sizes and shapes of the cold rolled specimen are very different from those of the AM specimens, and other mechanisms may also be contributing to sensitization depth.

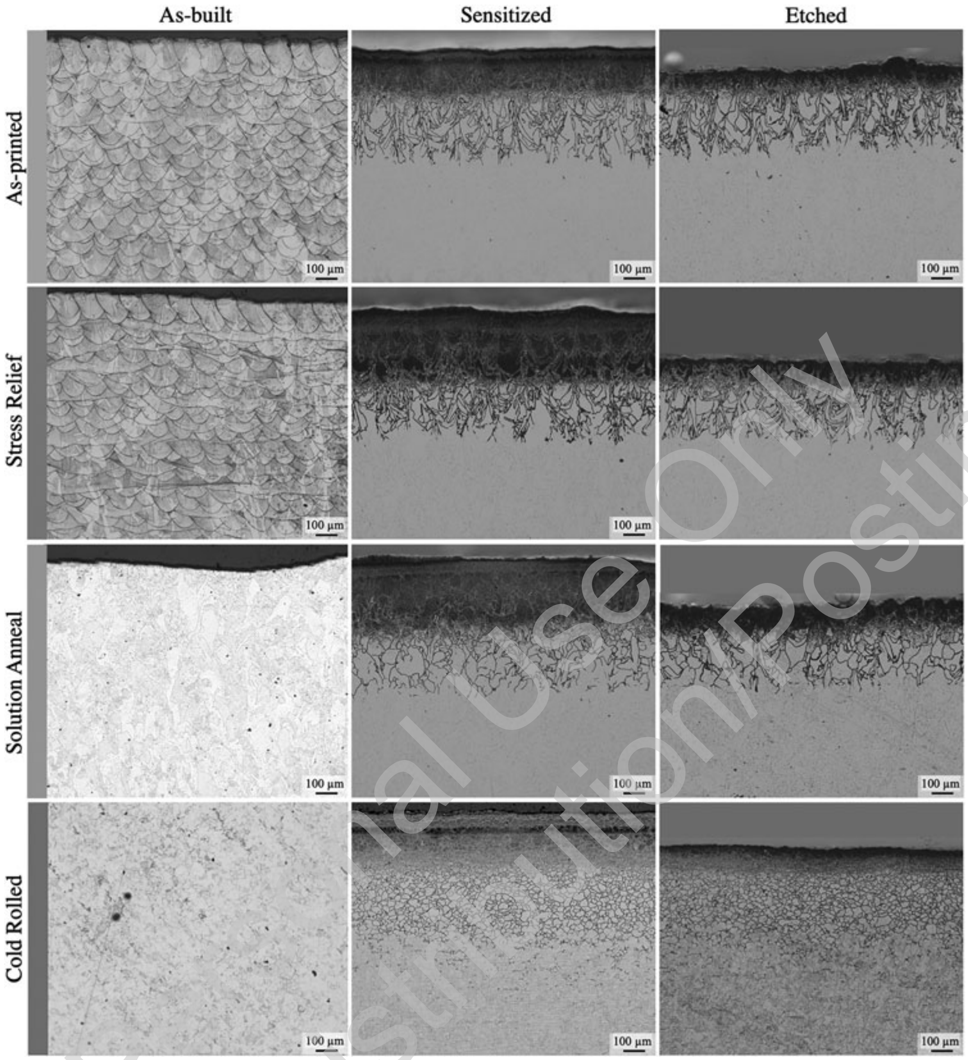

FIG. 2. 6.3 · Cross-sectional micrographs depicting the as-built microstructures, sensitized specimens' carbon diffusion lengths, and etched specimens' carbon diffusion lengths. Intra- and intergranular diffusion is noted for both sensitized and etched specimens, with the etched micrographs depicting the amount of material removed from the surface.

Intergranular diffusion length increases with increasing AB dislocation density. The AP specimen's intergranular diffusion length is 261 lm, followed by the SR specimen's intergranular diffusion length of 218 lm and the SA specimen's intergranular diffusion length of 200 lm. This is also consistent with a previous finding that increasing strain promotes intergranular precipitation.[29]

Grain coarsening also decreases the intergranular carbide diffusion length since grain boundaries are a dominant path for diffusing species,[13] and larger grain sizes result in a smaller grain boundary volume, therefore limiting the amount of slow-diffusing carbon into the bulk. Li et al have previously shown that smaller grains promote intergranular chromium carbide precipitation in conventional 316L stainless steel, with the degree of sensitization decreasing as grains coarsen.[30]

The SIMS results support the observation of carbon movement along dislocations. Figure 4a–c shows the normalized intensity of the carbon ion, C$^-$, measured through SIMS from the edge (starting at 0 lm) to the bulk of the AP-S, SR-S, and SA-S specimens, respectively. Figure 4a includes the curve for the cold rolled control for comparison. Dashed lines represent the normalized intensity at the point where the etching terminated, the results of which are discussed in the next section of this article.

All curves depict the same general features—initially, a peak in normalized intensity from 0 to *50 lm (depending on the specimen) is followed by a relatively horizontal region denoting uniform carbon intensity. This region, as described later, corresponds to the region etched in the second stage of the STEP. Next, there is an abrupt change in slope as the C$^-$ intensity decreases through the remainder of the intragranular region. Finally, the slope changes again, becoming shallower, as intergranular diffusion dominates. For reference, these features are also noted in the micrographs included above each specimen's plot.

In Figure 4a, the initial peak of the AP-S curve begins at the highest normalized intensity, indicating that dislocations enable relatively rapid diffusion of carbon into the bulk. Next, the horizontal region occurs at approximately twice the normalized intensity as the corresponding regions in the SR-S and SA-S curves—this suggests a greater concentration of carbon in the intragranular region, supporting the theory of carbon diffusion along dislocations into the bulk.

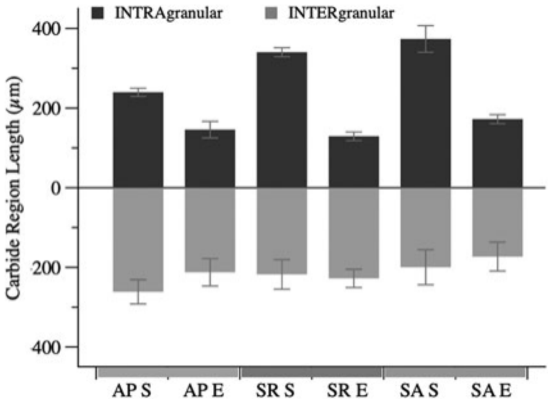

FIG. 3. Numerical depiction of the intra- and intergranular carbide region lengths for each specimen at each stage in the STEP. The differences in intragranular length between the same specimen types indicate material removal. STEP, self-terminating etching process.

Additionally, the AP-S specimen's smaller grain size provides a larger grain boundary volume to further assist in diffusion of carbon. The combined result is a short intragranular region having a high carbon content and a longer intergranular region with a relatively high normalized intensity of carbon. The lowest dislocation density and coarser grained SA-S specimen (Fig. 4c) exhibits the opposite effect. The normalized intensity of carbon is lower and more disperse across a longer intragranular region due to fewer dislocations for the carbon to use to diffuse into the grains; aided by a smaller grain boundary volume, the intergranular diffusion depth is the shortest of all evaluated specimens.

Near the edge, the SR-S (Fig. 4b) curve follows a similar behavior to the AP-S curve, having a similar normalized intensity of C^- from the edge to *100 lm, as the dislocations enable carbon transport into the grains. From there, the SR-S curve behaves more similarly to the SA-S curve and then tapers off to a normalized intensity of nearly zero by the end of the intergranular region.

`Etched specimens.` The lack of applied heat during the etching portion of the STEP retained the microstructures from the sensitized condition. However, the micrographs of the etched specimens do reveal varying reductions in the intragranular carbide regions. As depicted in Figure 3, the SR-E specimen had the shortest depth of sensitized region remaining on the surface postetching. The amount of sensitized material remaining at the conclusion of the STEP is important since it can be detrimental to the corrosion reliability of the processed part.[4]

Figure 5 shows the total material removed, calculated by subtracting the intragranular diffusion length of etched specimens from that of sensitized specimens. The most amount of material was removed through chemical etching from the SA specimen (228 lm); for the largest range in support structure dimensions that can be removed, pre-STEP solution annealing should be conducted.

The least amount of material was removed from the AP specimen (143 lm). Over 50 lm more material was removed from the SR specimen than the AP specimen (201 lm); these findings are thus supportive of material removal not corresponding strictly to microstructure, but rather other factors such as carbon concentration.

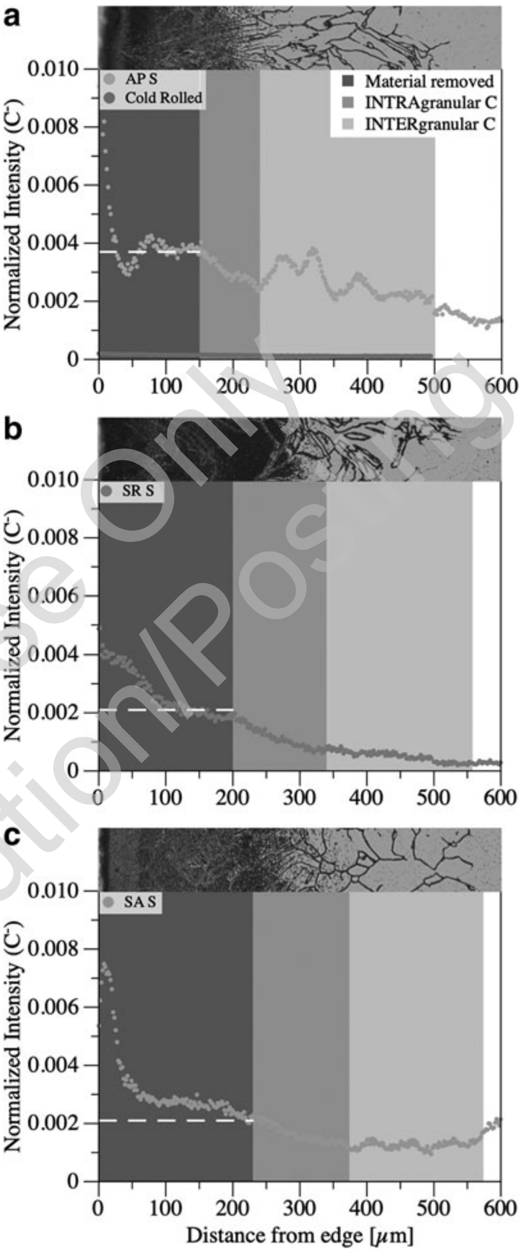

FIG. 4. Normalized intensity curves for C^- in the (a) AP-S, (b) SR-S, and (c) SA-S specimens from the edges into the bulk measured through SIMS. The normalized intensity of carbon across the AP-S specimen is higher due to carbon diffusion along dislocations. Diffusion through the SR-S and SA-S specimens is impeded by fewer dislocations and larger grain size reducing grain boundary volume.

In Figure 4a–c, the darkest shading on the far left of each graph delineates the region of material removed. The dashed horizontal lines indicate the normalized intensity of C^- when the etching process terminated. Notably, the material removal terminates at depths corresponding to slope inflection points in the intensity curves. For example, in Figure 4a and b, for the AP-S and SR-S carbon curves, respectively, material removal terminates immediately preceding a steepening of the slope, indicating a decrease in normalized intensity and, ultimately, decreasing carbon concentration.

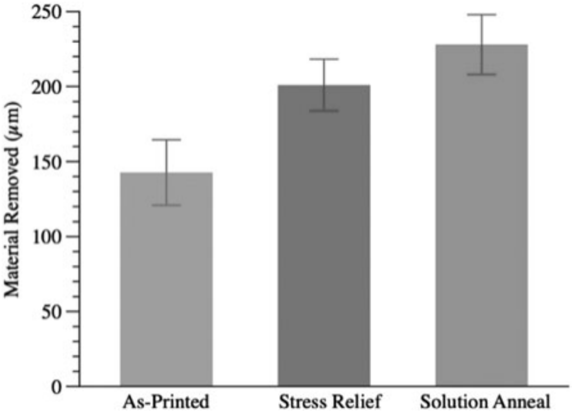

FIG. 5. Total material removed from the intragranular carbon diffusion region following the STEP.

For the SA-S specimen (Fig. 4c), etching terminates when the normalized carbon concentration decreases to *0.002, which is the same normalized intensity that SR-S etching terminates at. AP-S specimen etching terminates at a slightly higher normalized intensity of *0.0037; however, for this specimen, the intragranular region terminates at 0.002.

While the content of carbon is high in the AP-S specimen, it does not necessarily equate to a high content of carbides, which are etched during the STEP. As noted by Kalish and Cohen, high dislocation densities can attract and trap carbon, subsequently inhibiting the formation of carbides.[31]

Therefore, material removal may terminate once the carbide concentration decreases beyond a certain value despite some specimens having excess C⁻ content as signified by the SIMS analysis. Additionally, the amount of material removed increases with grain size since (as discussed later in the article) material removal preferentially terminates at grain boundaries.

A rough estimation of the C⁻ concentration for the AP-S, SR-S, and SA-S specimens may be possible with the initial C⁻ (ion) concentration of the AP-AB specimen, but only the elemental C concentration is known. However, we know it is above 0.03%, the commonly regarded value beyond which steel becomes susceptible to intergranular corrosion.[32] A much deeper evaluation of SIMS data, including quantification, represents significant future work.

Surface roughness

Surface roughness is an important parameter for parts in certain applications relying on tight geometric tolerance, wear performance,[33] and corrosion reliability,[34] among other considerations, including fatigue performance. Fatigue performance improves with decreasing surface roughness in both wrought and L-PBF metals.[35,36]

Hatami et al showed an improvement of 50 MPa in the fatigue performance of L-PBF 316L stainless steel when the surface was machined compared with the AB condition.[37] The authors' upcoming work will specifically address the effect of the STEP on fatigue performance of L-PBF 316L stainless steel. The current work evaluates how microstructural changes impact surface roughness.

As shown by Hoffman et al, applied bias in the STEP controls the resulting surface roughness of processed parts.[5] An applied bias of 550 mV_{SHE} resulted in uniform corrosion (intragranular and intergranular) across the surface, while a lower bias of 400 mV_{SHE} mostly attacked the grain boundaries, thus resulting in a comparatively rougher surface.

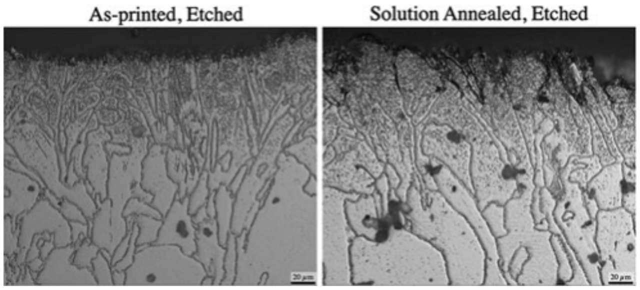

FIG. 6. 31.5 · Cross-sectional micrographs of the near-surface microstructure of AP-E (left) and SA-E (right) specimens. The finer grain structure of the AP-E specimen resulted in more uniform corrosion across the surface, while the corrosive attack accentuated the SA-E specimen's coarser structure. Specimens were stain etched with glyceregia for 80 s.

However, as depicted in Figure 6, the effect of using a larger bias to achieve more uniform corrosion is diminished when

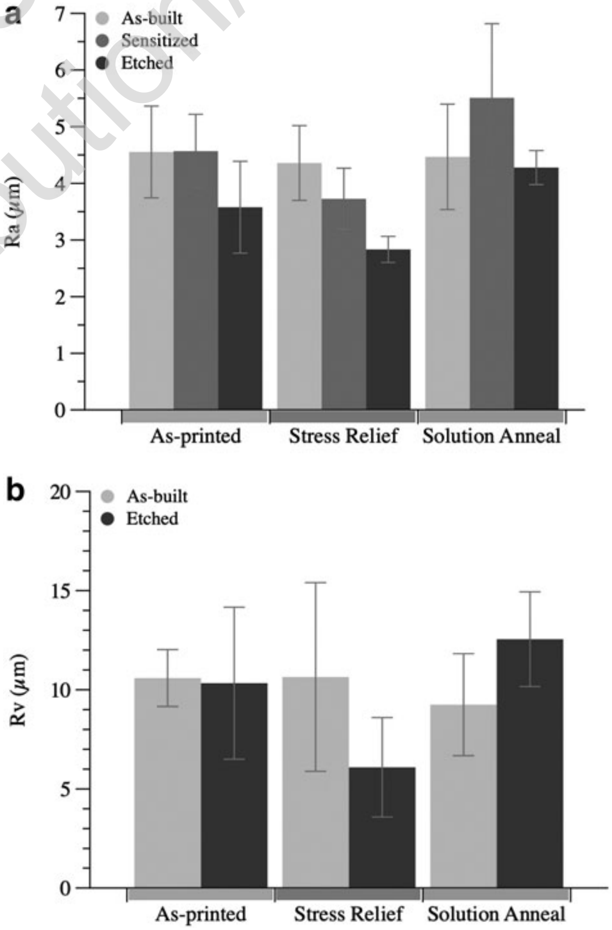

FIG. 7. (a) Evaluation of Ra surface roughness for all specimens. The SR specimen had the largest improvement in roughness from the as-built condition to etched condition. Generally, the STEP resulted in smoother surfaces for all specimen types. (b) Rv roughness derived from Ra. The SR specimen had the smallest average Rv and the SA specimen had the largest.

grains are coarsened through solution annealing; the figure shows preferential termination of intragranular corrosion mainly at grain boundaries of SA-E specimens, while the finer-grained AP-E microstructure better supports uniform material removal.

The profilometry results (Fig. 7) support this finding; SA-E specimens have the roughest surfaces of all chemically etched specimens, while AP-E and SR-E specimens had greater improvements in surface roughness from their AB (AP-AB and SR-AB) conditions.

All AB surfaces had similar starting roughness regardless of heat treatment, with the SR specimen having slightly lower initial Ra roughness. As previously noted, the STEP did result in an improvement in surface roughness between the AB and chemically etched conditions of all specimens. For the AP specimen, average Ra roughness decreased by nearly one micron, from 4.55 – 0.8 lm for the AB condition to 3.58 – 0.8 lm, after etching.

The SR specimen had the largest improvement in surface roughness with AB roughness of 4.36 – 0.7 lm decreasing to 2.83 – 0.2 lm after etching. The SA specimen's average Ra roughness decreased slightly from 4.47 – 0.9 to 4.28 – 0.3 lm. Rv roughness has been shown to trend with fatigue life, where fatigue life increases with decreasing Rv.[38]

Figure 7b indicates that pre-STEP stress relief results in the lowest average Rv roughness of *6.09 lm—nearly half that of the SA-E specimen's Rv roughness of 12.54 lm. For surface roughness optimization, a stress relief heat treatment is recommended before performing the STEP.

Conclusions

This work evaluated the effects of varying the dislocation density and initial microstructure of L-PBF 316L stainless steel on sensitization depth and material removed during a STEP, ultimately elucidating the impact on final surface roughness. The major findings of this work are as follows:

Sensitization depth increased with decreasing dislocation density, with the intragranular carbon diffusion depth being the shortest for the AP-S specimen due to enhanced carbon diffusion along dislocations. The SA-S specimen had the coarsest grains, lowest dislocation density, and longest diffusion length.

Material removal during etching terminated at a specific concentration of carbon and preferentially along grain boundaries. The SA specimen had the largest depth of material removed during etching.

The stress-relieved specimen had the lowest surface roughness and the shortest depth of sensitized surface material after etching, thus rendering pre-STEP stress relief the most optimal treatment for future work involving fatigue and corrosion studies.

The author's future work includes a comprehensive study of the fatigue performance of L-PBF 316L subjected to the STEP as well as a corrosion study. Future work should also involve evaluation methods to decarburize the parts post-STEP.

Authors' Contributions

All authors contributed to the study conception and design. Material preparation and data collection and analysis were performed by S.P. Collection and analysis of SIMS data were performed by M.W. The first draft of the manuscript was written by S.P., and all authors commented on previous versions of the manuscript. All authors read and approved the final manuscript. Conceptualization was done by S.P. and O.H. Methodology was done by S.P. Formal analysis and investigation were performed by S.P. and M.W. Writing—original draft preparation—was done by S.P. Writing—review and editing—was done by O.H. and M.W. Funding acquisition, resources, and supervision were performed by O.H. and S.P.

Author Disclosure Statement

The authors declare that there are no conflicts of interest.

Funding Information

This material makes use of the TOF-SIMS system at the Colorado School of Mines, which was supported by the National Science Foundation under Grant No. 1726898. This material is based upon work supported by the National Science Foundation under Grant No. CAREER 1944516.

References

1. Post B, Lind R, Lloyd V, et al. The Economics of Big Area Additive Manufacturing. In: 27th Annual International Solid Freeform Fabrication Symposium—An Additive Manufacturing Conference, Austin, Texas; 2016.
2. Lefky CS, Zucker B, Wright D, et al. Dissolvable supports in powder bed fusion-printed stainless steel. 3D Print Addit Manuf 2017;4(1):3–11; doi: 10.1089/3dp.2016.0043
3. Raikar S, Heilig M, Mamidanna A, et al. Self-terminating etching process for automated support removal and surface finishing of additively manufactured Ti-6Al-4 V. Addit Manuf 2021;37:101694; doi: 10.1016/j.addma.2020.101694
4. Lefky C. Corrosion and Sensitized Microstructure Evolution of 3D Printed Stainless Steel 316 and Inconel 718 Dissolvable Supports. Arizona State University: Tempe, AZ, USA; 2018.
5. Hoffman R, Hinnebusch S, Raikar S, et al. Support thickness, pitch, and applied bias effects on the carbide formation, surface roughness, and material removal of additively manufactured 316 L stainless steel. JOM 2020;72:4254–4263; doi: 10.1007/s11837-020-04422-y
6. Saeidi K, Gao X, Zhong Y, et al. Hardened austenite steel with columnar sub-grain structure formed by laser melting. Mater Sci Eng A 2015;625:221–229; doi: 10.1016/j.msea.2014.12.018
7. Wang X, Muñiz-Lerma JA, Sánchez-Mata O, et al. Microstructure and mechanical properties of stainless steel 316L vertical struts manufactured by laser powder bed fusion process. Mater Sci Eng A 2018;736:27–40; doi: 10.1016/j.msea.2018.08.069
8. Prochaska S, Hildreth O. Effect of chemically accelerated vibratory finishing on the corrosion behavior of laser powder bed fusion 316 L stainless steel. J Mater Process Technol 2022;305:117596; doi: 10.1016/j.jmatprotec.2022.117596
9. Sprouster DJ, Streit Cunningham W, Halada GP, et al. Dislocation microstructure and its influence on corrosion behavior in laser additively manufactured 316L stainless steel. Addit Manuf 2021;47:102263; doi: 10.1016/j.addma.2021.102263
10. Sprengel M, Ulbricht A, Evans A, et al. Towards the optimization of post-laser powder bed fusion stress-relieve treatments of stainless steel 316L. Metall Mater Trans A 2021;52(12):5342–5356; doi: 10.1007/s11661-021-06472-6

11. Chyrkin A, Huczkowski P, Shemet V, et al. Sub-scale depletion and enrichment processes during high temperature oxidation of the nickel base alloy 625 in the temperature range 900–1000°C. Oxid Met 2011;75(3–4):143–166; doi: 10.1007/s11085-010-9225-3
12. Xie R, Lu S, Li W, et al. Dissociated dislocation-mediated carbon transport and diffusion in austenitic iron. Acta Mater 2020;191:43–50; doi: 10.1016/j.actamat.2020.03.042
13. Balluffi RW, Allen SM, Carter WC. Kinetics of Materials: Balluffi/Kinetics. John Wiley & Sons, Inc.: Hoboken, NJ, USA; 2005.
14. Sohrabpoor H, Salarvand V, Lupoi R, et al. Microstructural and mechanical evaluation of post-processed SS 316L manufactured by laser-based powder bed fusion. J Mater Res Technol 2021;12:210–220; doi: 10.1016/j.jmrt.2021.02.090
15. Davis JR, ASM International, (eds). Metals Handbook. Desk ed., 2nd ed. ASM International: Materials Park, OH, USA; 1998.
16. ASTM International. ASTM F3184-16, Standard Specification for Additive Manufacturing Stainless Steel Alloy (UNS S31603) with Powder Bed Fusion. ASTM International: West Conshohocken, PA, USA; 2016.
17. Rai SK, Kumar A, Shankar V, et al. Characterization of microstructures in Inconel 625 using X-ray diffraction peak broadening and lattice parameter measurements. Scr Mater 2004;51(1):59–63; doi: 10.1016/j.scriptamat.2004.03.017
18. Rietveld HM. A profile refinement method for nuclear and magnetic structures. J Appl Crystallogr 1969;2(2):65–71; doi: 10.1107/S0021889869006558
19. Hall WH. X-ray line broadening in metals. Proc Phys Soc 1949;Section A(62):741.
20. Williamson GK, Smallman RE. III. Dislocation densities in some annealed and cold-worked metals from measurements on the X-ray debye-scherrer spectrum. Philos Mag 1956;1(1):34–46; doi: 10.1080/14786435608238074
21. Peng Y, Gong J, Jiang Y, et al. The effect of plastic prestrain on low-temperature surface carburization of AISI 304 austenitic stainless steel. Surf Coat Technol 2016;304:16–22; doi: 10.1016/j.surfcoat.2016.05.047
22. ASM International, Handbook Committee. ASM Handbook. Volume 9. ASM International: Materials Park, OH, USA; 2004.
23. International Organization for Standardization. ISO 4287:1997 Geometrical Product Specifications (GPS)—Surface Texture: Profile Method—Terms, Definitions and Surface Texture Parameters. International Organization for Standardization; 2015.
24. Yoshie A, Fujita T, Fujioka M, et al. Formation of the Decrease in Dislocation Density of Deformed Austenite Due to Static Recovery and Recrystallization. ISIJ Int 1996;36(4):474–480; doi: 10.2355/isijinternational.36.474
25. Kohnert A, Capolungo L. The kinetics of static recovery by dislocation climb. Npj Comput Mater 2022;8:104; doi: 10.1038/s41524-022-00790-y
26. Saha DC, Biro E, Gerlich AP, et al. Effects of tempering mode on the structural changes of martensite. Mater Sci Eng A 2016;673:467–475; doi: 10.1016/j.msea.2016.07.092
27. Advani AH, Murr LE, Atteridge DG, et al. Deformation effects on intragranular carbide precipitation and transgranular chromium depletion in type 316 stainless steels. Corrosion 1991;47(12):939–947; doi: 10.5006/1.3585206
28. Salarvand V, Sohrabpoor H, Mohammadi MA, et al. Microstructure and corrosion evaluation of as-built and heat-treated 316L stainless steel manufactured by laser powder bed fusion. J Mater Res Technol 2022;18:4104–4113; doi: 10.1016/j.jmrt.2022.03.156
29. Oh YJ, Hong JH. Nitrogen effect on precipitation and sensitization in cold-worked Type 316L(N) stainless steels. J Nucl Mater 2000;278(2–3):242–250; doi: 10.1016/S0022-3115(99)00255-X
30. Li S-X, He Y-N, Yu S-R, et al. Evaluation of the effect of grain size on chromium carbide precipitation and intergranular corrosion of 316L stainless steel. Corros Sci 2013;66:211–216; doi: 10.1016/j.corsci.2012.09.022
31. Kalish D, Cohen M. Structural changes and strengthening in the strain tempering of martensite. Mater Sci Eng 1970;6:156–166.
32. Kolli S, Ohligschläger T, Kömi J, et al. Sensitization and self-healing in austenitic stainless steel: Quantitative prediction considering carbide nucleation and growth. ISIJ Int 2019;59(11):2090–2097; doi: 10.2355/isijinternational.ISIJINT-2019-264
33. Guenther E, Kahlert M, Vollmer M, et al. Tribological performance of additively manufactured AISI H13 steel in different surface conditions. Materials 2021;14(4):928; doi: 10.3390/ma14040928
34. Melia MA, Duran JG, Koepke JR, et al. How build angle and post-processing impact roughness and corrosion of additively manufactured 316L stainless steel. Npj Mater Degrad 2020;4(1):21; doi: 10.1038/s41529-020-00126-5
35. Javadi H, Jomaa W, Texier D, et al. Surface roughness effects on the fatigue behavior of as-machined Inconel718. Solid State Phenom 2016;258:306–309; doi: 10.4028/www.scientific.net/SSP.258.306
36. Pegues J, Roach M, Scott Williamson R, et al. Surface roughness effects on the fatigue strength of additively manufactured Ti-6Al-4V. Int J Fatigue 2018;116:543–552; doi: 10.1016/j.ijfatigue.2018.07.013
37. Hatami S, Ma T, Vuoristo T, et al. Fatigue strength of 316 L stainless steel manufactured by selective laser melting. J Mater Eng Perform 2020;29(5):3183–3194; doi: 10.1007/s11665-020-04859-x.
38. Gockel J, Sheridan L, Koerper B, et al. The influence of additive manufacturing processing parameters on surface roughness and fatigue life. Int J Fatigue 2019;124:380–388; doi: 10.1016/j.ijfatigue.2019.03.025

Address correspondence to:
Owen Hildreth
Department of Mechanical Engineering
Colorado School of Mines
1500 Illinois Street
Golden, CO 80401
USA

E-mail: ohildreth@mines.edu